Dual Injection in Supersonic Crossflow: Analysis Jet Shear Layer from Schlieren Images

Jan Siemen Smink,* Harry W. M. Hoeijmakers,† and Cornelis H. Venner‡
University of Twente, 7500 AE Enschede, The Netherlands

https://doi.org/10.2514/1.J061843

In supersonic-combustion ramjets (scramjets), fuel is injected, which should mix rapidly with the supersonic crossflow to minimize the length of the scramjet. Tandem dual-jet injection has shown improved mixing performance over single-jet injection. However, experiments on tandem dual-jet injection have not addressed the jet shear layer, in which the mixing occurs, yet. The present study investigates the jet shear layer, as well as the bow shocks in front of the jets, in a continuous air-indraft supersonic wind tunnel at Mach number 1.55. A schlieren setup has been used for visualizing the flow features. A largely automated algorithm for processing schlieren images has been developed to determine the location of the upper boundary of the jet shear layer. The penetration of the jet is studied as a function of 1) J, the ratio of the momentum of the jet and that of the crossflow, and 2) the dimensionless distance S between the dual-jets. An empirical similarity relation has been established for the time-averaged location of the jet upper shear layer as function of J and S, covering the investigated conditions ($J \in [2.8,3.8,4.8]$, $S \in [0:9.87]$). This empirical similarity relation provides S_{opt}, the spacing for maximal penetration of the jets as function of J.

I. Introduction

As A result of increased power of propulsion systems, flight speeds have increased accordingly. At present, because of high fuel consumption and regulations on the generation of sonic booms in supersonic flight, civil aviation concerns subsonic/transonic flight only. However, military aircraft, such as the F-35 Lightning II, operate at moderate supersonic speeds.

To achieve high supersonic flight velocities, appropriate propulsion systems are required. Airbreathing propulsion systems use oxygen from the freestream air for combustion of fuel. In jet engines, the supersonic freestream is decelerated to a lower Mach number through a converging channel in which the pressure and temperature increase. In the resulting high-temperature, high-pressure flow, gaseous fuel injection and ignition take place. Subsequently, the exhaust mixture passes through a nozzle in which the mixture accelerates to high supersonic speed and finally is ejected in downstream direction to provide forward thrust to the aircraft.

Jet engines are optimized for a certain range of flight speeds. In ramjets, used in the range of flight speeds Mach 2 to Mach 6, air is compressed using the so-called ram effect. The air decelerates to subsonic speed in the combustor, where fuel is mixed in the airflow and ignited. For flight speeds exceeding Mach 5, ramjets are not effective because the flow deceleration to subsonic speed results in a too-large temperature rise and consequently in a low efficiency of combustion. For this reason, at hypersonic speeds ($5 < M < 12$), scramjets (supersonic combustion ramjets) are used; see Fig. 1. In scramjets, the flow is decelerated, from a high to a lower, but still supersonic, Mach number; fuel injection and mixing then take place in supersonic flow at optimal thermodynamic conditions. Injection into a supersonic crossflow is complicated by the relative short length available for mixing as well as by flow features such as shock waves [1].

Presented as Paper 2022-2565 at AIAA SciTech 2022 Forum, San Diego, CA & Virtual, January 3–7, 2022; received 14 March 2022; revision received 11 June 2022; accepted for publication 23 July 2022; published online 7 September 2022.

*Ph.D. Student, Faculty Engineering Technology, Group Engineering Fluid Dynamics, P.O. Box 217.

†Professor, Faculty Engineering Technology, Group Engineering Fluid Dynamics, P.O. Box 217. Senior Member AIAA.

‡Professor, Faculty Engineering Technology, Group Engineering Fluid Dynamics, P.O. Box 217. Member AIAA.

The focus of the present study is on the flow features that have an effect on the efficiency of mixing in a scramjet engine. An efficient combustion process requires rapid mixing of fuel with the airflow, while preserving the momentum of the airflow as much as possible. To enhance mixing, fuel is injected transversely into the supersonic crossflow, facilitating the combustion process to occur within a relatively short distance. In this way, also inside the scramjet, the skin friction drag, which is significant at high speed, is kept within bounds.

Preceding research [2,3–5] on tandem dual injection into supersonic crossflow has shown enhanced penetration and mixing in comparison to single-jet injection. The present study pursues further research on tandem dual-jet injection into supersonic crossflow.

Figure 2 gives a schematic view of the main structure in the flow with dual-jet injection. When transversely injecting gas into a supersonic crossflow, a bow shock arises in front of the jet. The bow shock decreases the momentum in the crossflow, which allows the jet to penetrate deeper into the crossflow [4]. In tandem dual-jet injection, an additional bow shock arises in front of the downstream jet. Under certain conditions, the two bow shocks can merge [2]. However, neither the required conditions for this to occur nor the effect of the two shocks on the penetration of the jet is clear. In the present study, the aim is to investigate whether the merging of the bow shocks has an influence on the penetration in dual sonic jet injection.

Many studies have been carried out into single-jet injection into a supersonic crossflow (e.g., Refs. [6–10]). A measure for the penetration of the transversely injected jet is the location of its upper edge, the so-called jet upper shear layer. This shear layer features large-scale structures, which enhance the mixing of the gas from the jet with the gas of the crossflow, resulting in deeper penetration of the jet.

From the parametric investigations of Schetz and Billig [6], Papamoschou and Hubbard [7], and Portz and Segal [8] for single-jet injection, it is known that the location y/D_t of the jet upper shear layer as a function of dimensionless distance x/D_t from the downstream orifice (with D_t the so-called total diameter) mainly depends on J, the jet-to-crossflow momentum flux ratio (to be defined in Sec. II.A), and on M_c, the crossflow Mach number. When considering tandem dual-jet injection, the dimensionless distance S between the two orifices (to be defined in Sec. II.A) has a major effect on the penetration of the jet [2].

For single-jet injection, literature provides empirical power-law relations for the location of the jet upper shear layer, e.g., the work of Gruber et al. [10,11] and Rothstein and Wantuck [12]. For tandem dual-jet injection, de Maag et al. [2] found empirical power-law relations in the form of $y/D_t = c_1(x/D_t - c_3)^{c_2}$.

Landsberg [4] carried out a numerical study into tandem dual jet injection of hydrogen into a supersonic crossflow, which, in

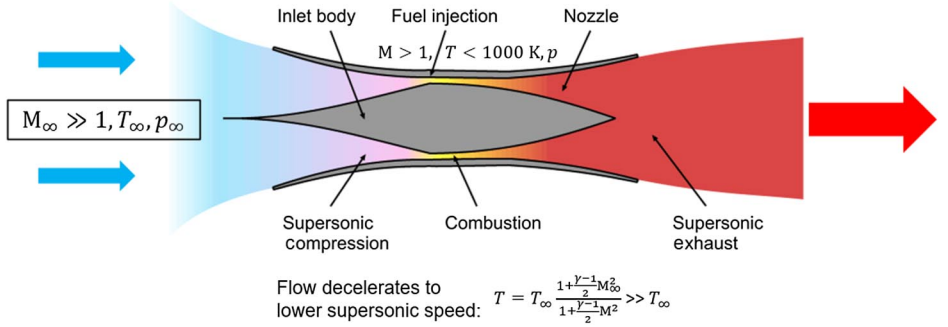

Fig. 1 Schematic of a scramjet in which flow is supersonic throughout whole engine. Adapted with permission from Ref. [2] (copyright 2020 by AIAA).

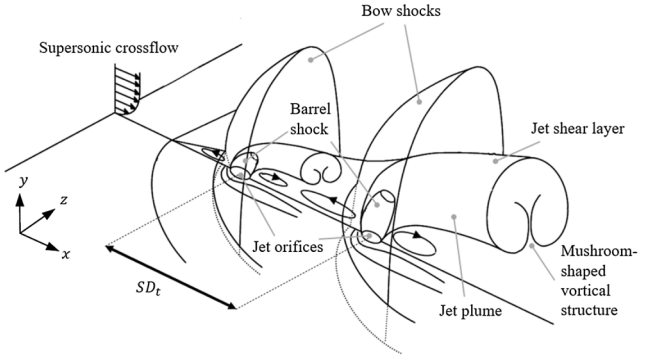

Fig. 2 Schematic of tandem dual sonic jet injection into supersonic crossflow. Adapted with permission from Ref. [3] (copyright 2006 by AIAA).

comparison with single-jet injection, showed an enhancement of the penetration of the jet upper shear layer. For fixed values of J and M_c, an optimal distance S at which penetration is maximal was observed. This has been confirmed in the numerical study of Lee [3] and the experimental study of de Maag et al. [2]. Furthermore, Landsberg observed the dependency of the location of the jet upper shear layer on the crossflow Mach number M_c. An increased crossflow Mach number results in increased near-field ($x/D_t < 15$) penetration but a decreased far-field penetration ($x/D_t > 15$). Landsberg explains that this is caused by the loss in vertical momentum in the jet, which is induced by the stronger barrel shock associated with the deeper underexpansion of the jet in the crossflow of higher Mach number.

While Landsberg varied M_c and S, Lee [3] investigated the effect of variation of J and S on the penetration due to tandem dual-jet injection. J determines the extent of the blockage of the crossflow by the jets. The larger J is, the stronger the bow shocks become, and the stronger the blockage is. The upstream jet partly blocks the crossflow, such that the downstream jet can penetrate deeper into the crossflow. Thus, near-field penetration should increase with increasing J, and an optimal value of the penetration for some value of S is expected.

De Maag et al. [2,5] experimentally investigated tandem dual-jet injection of air into a supersonic crossflow of air. In that study, similar to the work of Lee [3], the effects of J and S on penetration were investigated at constant M_c, but only in the near-field domain. From schlieren images, the time-averaged location of the jet upper shear layer was captured, as a function of downstream distance, in a three-coefficient fit, with J and S as parameters. In addition, de Maag et al. carried out a similarity analysis by scaling the relations in terms of J at constant S. However, the role of S in these empirical similarity relations remained unaddressed.

In the present study, the effect of the dual distance S and the jet-to-crossflow momentum flux ratio J on the location of the jet shear layer, as well as the characteristics of the bow shocks, are investigated experimentally. Section II.A describes the experimental setup for acquiring schlieren images. Section II.B presents the semi-automatic algorithm for postprocessing the images, which results in the data that have been used in the analysis of the jet upper shear layer. Subsequently, Sec. III.A describes the characteristics of the bow shocks that form in front of the jets, and Sec. III.B analyzes the jet upper shear layer, resulting in similarity relations for the time-averaged location of the jet upper shear layer y/D_t as function of x/D_t, J, and S.

II. Methodology

A. Experimental Setup

The experiments have been carried out in the Supersonic Wind Tunnel facility at the University of Twente (Fig. 3). A 96 kW Kaeser Omega vacuum pump drives this air indraft wind tunnel, generating a subatmospheric pressure in the downstream part of the wind tunnel. Atmospheric air is pulled through a throat where the flow becomes sonic. In the divergent channel downstream of the throat, the flow turns supersonic. The cross-sectional area in the divergent channel is adjustable such that speeds up to $M_c = 1.7$ can be achieved. In the present study, the speed is set to reach $M_c = 1.55 \pm 0.02$ in the test section of cross-section $45 \pm 0.5 \times 47.9 \pm 0.5$ mm (width × height). Figure 3 shows a photograph of the wind tunnel setup and measurement equipment used. Figure 4 shows a schematic of the side view of the test section.

The inlet of the wind tunnel (left) is at atmospheric conditions, providing the total temperature $T_{0,c}$ and the total pressure $p_{0,c}$. Perpendicular to the bottom wall, pressurized air is injected at sonic speed from two (tandem) orifices. The air in the jet(s) originates from a plenum in which the total pressure of the jet flow is measured using a single plenum GE Druck DP 104 pressure sensor. For tandem dual-jet injection, air is injected into the crossflow through two orifices with diameters $D_1 = 1$ mm and $D_2 = 2$ mm, respectively. This results in $D_1/D_2 = 0.5$ and a total diameter of $D_t \equiv \sqrt{D_1^2 + D_2^2} = \sqrt{5}$ mm. For single-jet injection, air is injected through a single orifice, with diameter $D = D_t = \sqrt{5}$ mm, chosen to be equal to the total diameter

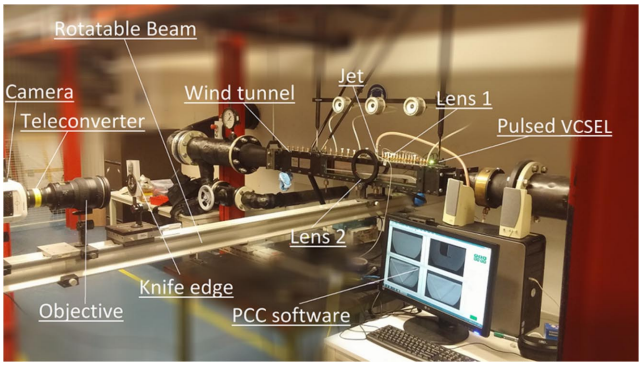

Fig. 3 Supersonic wind-tunnel facility with schlieren setup at University of Twente. Adapted with permission from Ref. [2] (copyright 2020 by AIAA).

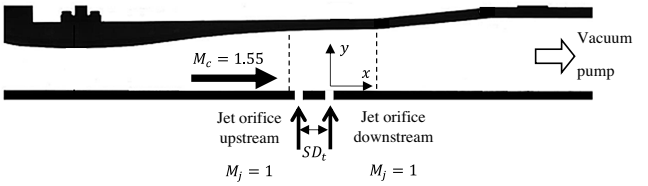

Fig. 4 Schematic of side view test section supersonic wind tunnel at University of Twente [5]. The test section, marked by dashed lines, is slightly divergent, which corrects for effect of vertical boundary layer.

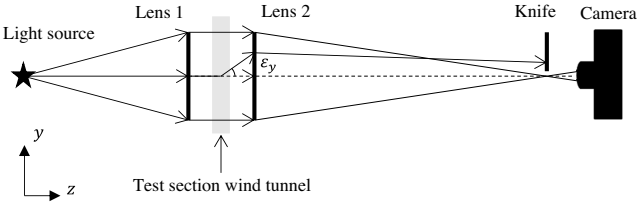

Fig. 5 Schematic overview of present schlieren setup. The left and right walls of the test section are glass windows.

D_t of the orifices for tandem dual-jet injection. Therefore, the sonic single-jet and sonic dual-jet injection are equivalent with respect to the injected mass flow.

For dual-jet injection, the distance between the centerlines of the two orifices is Δx. The nondimensionalized dual distance S is defined as

$$S \equiv \frac{\Delta x}{D_t} \tag{1}$$

The investigated parameter space is $\Delta x \in [8, 9, 10, 11, 12, 13, 14, 16, 19, 22]$, corresponding to $S \in [3.59, 4.04, 4.48, 4.93, 5.38, 5.83, 6.28, 7.17, 8.52, 9.87]$.

In the present investigation, the sonic jet injection is characterized by J, in other words, the jet-to-crossflow momentum flux ratio. This dimensionless number is, for calorically perfect gases, given by

$$J = \frac{\gamma_j p_{0,j} M_j^2 [1 + (1/2)(\gamma_c - 1) M_c^2]^{\gamma_c/(\gamma_c - 1)}}{\gamma_c p_{0,c} M_c^2 [1 + (1/2)(\gamma_j - 1) M_j^2]^{\gamma_j/(\gamma_j - 1)}} \tag{2}$$

The subscripts j and c correspond to jet and crossflow, respectively; γ is the ratio of specific heats; M is the Mach number; and p_0 is the total pressure. All quantities in Eq. (2) are easily measured.

Experiments for $J = 2.8$ and $J = 3.8$ have been carried out for the whole range of S. In addition, for $S = 0$ (single-jet) and $S = 5.38$, experiments have been carried out for a higher value of J, namely, $J = 4.8$. Because the similarity relations are derived from data for $J = 2.8$ and $J = 3.8$, the measurement for $J = 4.8$ provides data for verification of the empirical relations for a higher value of J. Furthermore, de Maag et al. [2] provided complementary data for three lower values of J, namely, $J = 1.0$, 1.4, and 2.0 and a slightly different set of values of S, which, in the present study, was used to extend the verification of the empirical similarity relations to lower values of J.

Table 1 gives an overview of the conditions in the test section. Note that T_0, p_0, and M_c are measured, while the other parameters listed are derived from (isentropic) relations for calorically perfect gases. The underexpanded jet is at sonic speed, so therefore M_j is equal to 1.

Table 1 Conditions in test section for injection into supersonic crossflow (left) and in jet (right) (T_0, p_0, and M are measured, and all other quantities are calculated from isentropic relations for calorically perfect gases)

Conditions crossflow			Conditions jet		
$T_{0,c}$	292 ± 2	K	$T_{0,j}$	292 ± 2	K
$p_{0,c}$	101.325 ± 1	kPa	$p_{0,j}$	$330,443,558 \pm 1$	kPa
M_c	1.55 ± 0.02		M_j	1	
			J	2.8, 3.8, 4.8	
a_c	281.5 ± 2.5	m/s	a_j	312.7 ± 1.5	m/s
u_c	436.3 ± 10	m/s	u_j	312.7 ± 1.5	m/s
T_c	197 ± 3	K	T_j	243 ± 2	K
p_c	25.66 ± 1	kPa	p_j	$174,234,295 \pm 1$	kPa
γ_c	1.4		γ_j	1.4	

1. Schlieren Setup

The flow features in the test section are visualized using a schlieren setup. This qualitative technique makes use of the relation between variations in the density field and the refraction of light. Because deviations from the mean light intensity are induced by the refraction of light, the schlieren technique visualizes the density gradient in the medium in the form of a grayscale image. Figure 5 shows a schematic of the present schlieren setup. Light rays from the light source are converged by lens 1, with focal distance $f = 0.5$ m, into a parallel beam. Both lens 1 and the light source are outside the wind tunnel. The parallel beam enters the test section through the left glass wall perpendicularly and travels through the test section of the wind tunnel. The light rays in the beam refract when they pass through areas with a density gradient caused by flow features. Rays that do not interact with density gradients continue on their parallel paths.

At the other side of the wind tunnel, the remaining parallel light rays are converged by lens 2 with focal distance $f = 1.0$ m. A horizontal knife is placed near the focal point of lens 2, where the light rays that did not refract, focus. The knife-edge blocks the rays that do not pass through the focal point, so these rays are not included in the image. The remainder of the light beam ends up in the image, recorded by the Phantom V611 camera. The resulting schlieren image features shadows, which correspond to areas with density gradients in the test section [13]. The Phantom V611 camera is equipped with a Nikon TC-20 E AF-S Teleconverter II plus Nikkor AF-S 200 mm f/2.0 ED VR lens.

To facilitate high-quality schlieren imaging, a powerful light source is used: a Vertical-Cavity-Surface-Emitting Laser (VCSEL) from Tyson Technology. This VCSEL light source with a wavelength of $\lambda = 808$ nm was manufactured by the Optical Sciences group at the University of Twente; see Ref. [2]. It has a power of $P = 4.5$ W emitted from the laser surface of 1.19×1.19 mm. In the present experiments, the camera has a limited frame rate (1000 frames/s), resulting in a relatively long exposure time. This results in motion blur due to the rapidly propagating flow features. Preventing blur due to motion at the supersonic speed considered would require a typical frame rate of 1 million frames/s, which the present camera cannot achieve. Therefore, the wind-tunnel room is darkened, and the laser light is pulsed at a frequency of 1.0 kHz. This provides a reduction of the exposure time and accordingly prevents motion blur. The VCSEL used a pulse width of $T_p = 100$ ns, which is easily captured within the long period (990 μs) during which the shutter of the Phantom V611 is open. For more details of the light source, the reader is referred to Refs. [2,5].

B. Postprocessing of Schlieren Images

For every combination (J, S) considered, the schlieren images have been recorded. For capturing the frames recorded by the camera, the Phantom Camera Control® version 3.4 software of Phantom has been used. For postprocessing, a sequence of 20 images is extracted from the sequence of frames. The 20 images belonging to a certain sequence are treated by an identical setting of the postprocessing procedure. For this postprocessing procedure, MATLAB® R2020a has been used.

The purpose of the analysis is to investigate the characteristics of the effect of the flow of the dual sonic jet injected in the supersonic crossflow. Figure 6 shows an example of one of the schlieren images. In the figure, the different features (the barrel shock, bow

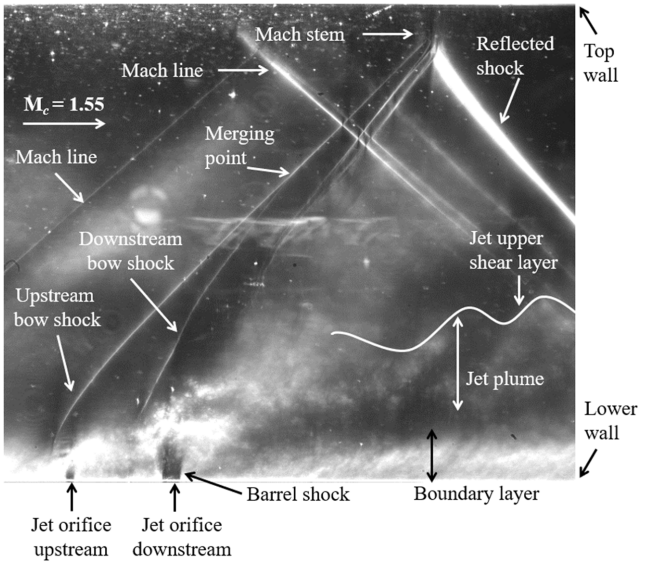

Fig. 6 Features of tandem dual sonic jet injection into supersonic cross-flow ($J = 3.8$, $S = 4.48$, and $M_c = 1.55$), shown in an unprocessed schlieren image.

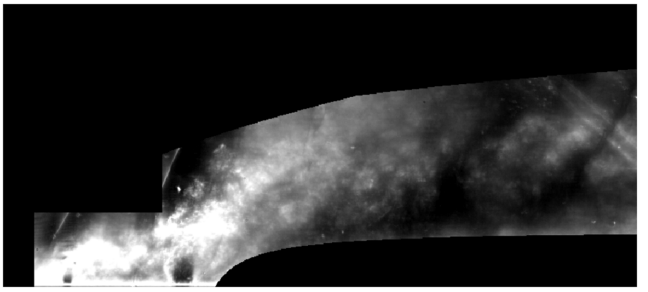

Fig. 7 Window (binary mask) determined within schlieren image. The window covers up areas not relevant for analysis of behavior of jet, areas that otherwise might disturb quality of results of postprocessing. ($J = 3.8$, $S = 4.93$, and $M_c = 1.55$).

shocks, jet plume, and reflected shock) observed in the flow during the experiments are identified. De Maag et al. [2] only analyzed four images per (J, S) combination visually. Though the jet upper shear layer (the upper side of the jet plume, so of regions with largely fluctuating flow) was detected, this method was labor intensive, while also the reliability of the results depended on the number of images used and on the visual detection procedure. For the present investigation, a largely automated postprocessing procedure has been developed which can handle a significantly larger number of images (20) per (J, S) combination within a reasonable amount of time.

For the detection of the jet upper shear layer, Lerink et al. [14] suggested an automatic procedure using MATLAB®'s Image Processing Toolbox. This method has served as a building block for the present postprocessing procedure. Kouchi et al. [15] also used a method to detect not only the upper edge of the shear layer but also the entire jet plume, in other words, the flow structures originating from the jet orifice. However, because Kouchi used subsequent images at small time intervals, for example, $\Delta t \sim 4$ μs, this method cannot be applied directly to the present experiments with $\Delta t \sim O(\text{ms})$. Still, some of the concepts used by Kouchi have been applied in the design of the present postprocessing algorithm. Flow structures are recurring with a period of order less than 10 μs. Therefore, these structures are captured with recording at $\Delta t \sim O(\text{ms})$, at random moments in a cycle, with adequate resolution when enough samples are taken.

The method for data processing consists of two main steps:

1) Determine a window, which provides a binary mask that excludes all nonrelevant parts of the image, in other words, parts which possibly generate noise in the desired data [14]. These parts are, for instance, the bow shocks, reflected shocks, and the boundary layer along the lower wall. Using image processing, the areas in the image with most time-varying light intensity are determined (bow shocks, boundary layer, jet plume, etc.) by comparing the image with a reference image. By exclusion of the bow shocks and the boundary layer, the region where the jet plume is located is identified. Restricting the original image to only this region results in the binary mask. For a result, see Fig. 7.

2) Identify the flow features in the jet, providing the data needed to determine the characteristics of the jet, especially the jet upper shear layer, which is the upper edge of the jet plume.

The window is determined once for each (J, S) combination considered and applied to the 20 images analyzed to reveal the characteristics of the jet for that combination. The images that are used have a size of approximately 800×600 pixels. For enhancement of the contrast and identification of the flow structures of the jet plume, each image is subjected to a number of processing steps. First, the local contrast within the image is increased using the MATLAB® function localcontrast (edge threshold: 0.3; enhancement 1, maximum). Second, the schlieren image is divided into five parts, such that the determination of the jet can be achieved optimally in each of the five separate parts. Each part is treated in the following manner: contrast is changed using the MATLAB® function imadjust, with automatic setting of the contrast limits. Thereafter, light intensity is uniformly distributed using the MATLAB® function histeq. For preventing noise amplification, the MATLAB® function adapthisteq is used for enhancing the local contrast (contrast enhancement limit: 0.4 ± 0.05, 8×16 tiles). Subsequently, the image is binarized using the MATLAB® function imbinarize (locally adaptive image threshold setting; sensitivity: 0.36 ± 0.04). Finally, the MATLAB® function bwmorph filters out noisy pixels (majority setting in 3×3 bits area). As a result, the dominant flow structures become visible (see Fig. 8 for an example of identification of slowly moving structures in the jet plume). For more details on the postprocessing procedure, see Ref. [16].

For each schlieren image, the flow features within the jet plume are captured as sets of coordinates. From the sets of coordinates of the clusters in a single image (see, e.g., Fig. 8), for every x coordinate, the corresponding y coordinates of the upper and lower edges of the plume are determined and stored as two additional sets of coordinates. Figure 9 illustrates the result for the upper and lower edges of the jet plume. Each image provides ± 350 data points for the upper edge and for the lower edge of the jet plume. Usually, the jet upper shear layer can be determined satisfactorily; however, because of the mushroom shape of the cross-section of the jet in the plane normal to the tunnel axis and because of the vortices forming in the jet plume, the location of the lower edge of the jet plume is not always well defined. For more details about the lower edge of the jet plume, see the work by Smink [17]. For each (J, S) combination, the sets of coordinates of all 20 schlieren images recorded are combined and stored for further analysis.

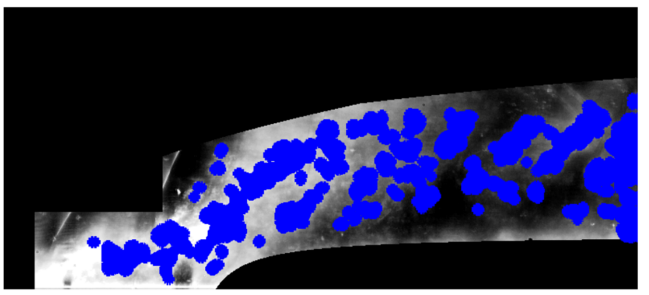

Fig. 8 Flow features in jet plume as determined from a schlieren image. Features in jet are indicated by clusters of closely spaced blue asterisks ($J = 3.8$, $S = 4.93$, and $M_c = 1.55$).

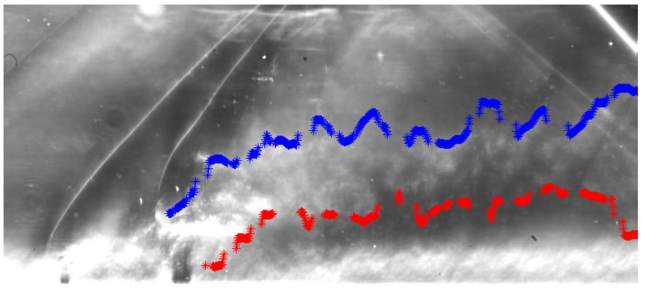

Fig. 9 Upper (blue) and lower (red) edge of jet plume upon application of postprocessing for a single schlieren image ($J = 3.8$, $S = 4.93$, and $M_c = 1.55$).

The data sets of the jet plume (set of coordinates shown in Fig. 8) can be used to generate a so-called isoincidence plot (see Fig. 10), in which the features in the jet are included as obtained from the combined twenty images. Data sets from figures such as Fig. 8 are superposed, and then per position the number of times the feature occurred is determined, which is defined as the incidence. The color at a specific location in the jet plume indicates the incidence, revealing either largely stationary, or frequently occurring, flow structures. For instance, in Fig. 10, the barrel shock just above the orifice of the downstream jet can be identified through the high values of the incidence (dark red color) in that region because it shows up in almost all of the 20 images processed.

In Sec. III.B, the data acquired for the jet upper shear layer are analyzed.

III. Results and Discussion

The experiments described in Sec. II.A have resulted in a large number of schlieren images. The Appendix (Figs. A1–A3) shows a sample image for each (J, S) combination investigated. For dual-jet injection, Fig. 6 already showed a schlieren image with the most relevant flow features indicated, while Fig. 2 showed the corresponding schematic representation of the flowfield.

Figure 6 shows that in front of each of the two jets from the bottom wall a bow shock is formed, which is reflected at the opposite wall of the test section. The position of the jet upper shear layer downstream of the second orifice is considered indicative for the penetration of the jet into the crossflow. It is also a measure for the extent the gas from the primary jet mixes with the gas from the crossflow. Note that the slope of the Mach lines, which are caused by small irregularities at the wind-tunnel walls, are a measure for the Mach number of the undisturbed crossflow: $\sin(\mu) = 1/M_c$, with μ the slope of the Mach line with respect to the horizon.

In the following subsections, the characteristics of the bow shocks and of the jet upper shear layer are analyzed. For that purpose, fits of the data are determined. The quality of these fits is assessed by the coefficient of determination R^2, defined as

$$R^2 \equiv 1 - \frac{\sum_{i=1}^{N}(f(x_i) - y_i)^2}{\sum_{i=1}^{N}(\bar{y} - y_i)^2} \quad \text{with} \quad \bar{y} = \frac{1}{N}\sum_{i=1}^{N} y_i \tag{3}$$

In this expression, (x_i, y_i), $i = 1, 2 \ldots N$, are the coordinates of N data points, $\bar{y}$ is the mean value of all y_i values, and $f(x_i)$ is the value of the fit evaluated at x_i. The specific fits used for the analysis are discussed in subsequent sections.

A. Characteristics of Bow Shocks

The characteristics of the bow shock upstream of each of the two jets have been investigated. Close to the jet orifice, the bow shock is nearly normal to the incoming flow, while farther from the orifice, the bow shock turns from a normal to an oblique shock. For the prevailing conditions, the refection of the oblique shock at the upper wall requires a normal shock, the so-called Mach stem. Time averaged, the downstream bow shock has a larger normal part near the jet orifice than the upstream bow shock because of the larger disturbance due to the larger mass flow $\dot{m}_2$ entering the flowfield through the downstream, primary, jet orifice compared to the mass flow $\dot{m}_1$ entering through the upstream jet orifice ($\dot{m}_1/\dot{m}_2 = 1/4$). In addition, the upstream bow shock slows down the flow, such that the downstream jet can bulge out farther.

The position of the bow shocks depends on the Mach number M_c of the crossflow, the jet-to-crossflow momentum flux ratio J, and the dual distance S. The crossflow Mach number determines the inclination of the oblique part of the bow shock, which is lower for higher Mach numbers. The spacing S between the orifices which determines the spacing between the bow shocks affects the shape of the bow shocks: the smaller the distance between the bow shocks is, the smaller the distance is from the lower wall at which they merge (see Fig. 11). Furthermore, a larger J results in a more extensive bulging out of the underexpanded sonic jet, resulting in a larger part of the bow shock being a normal shock. Further examples are found in the Appendix (Figs. A1–A3).

The schlieren images show that for specific combinations of J and S the two bow shocks merge. This point is called the merger point. The distance between the two bow shocks as well as whether or not the two bow shocks merge directly depends on J and S. The position of the merger point also depends on J and S; however, it is noted that the location of the merger point fluctuates due to significant time variation of the location of the downstream bow shock. The oscillatory character of the bow shocks was already observed in Refs. [9,18]. Gruber et al.

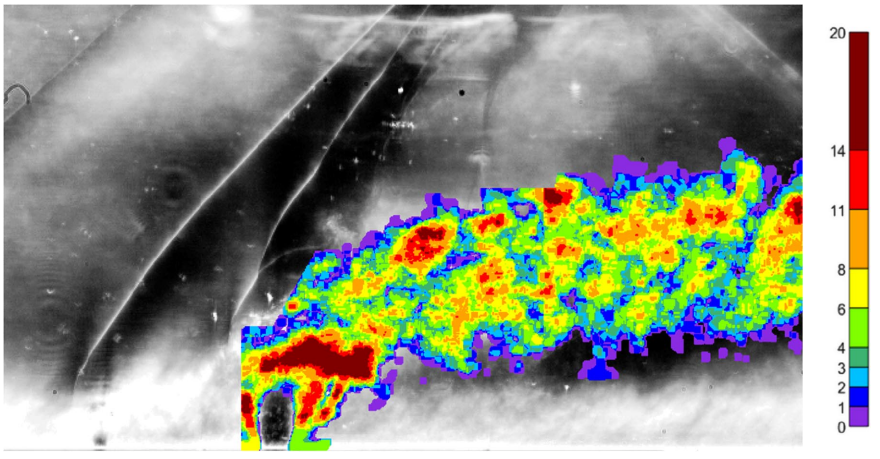

Fig. 10 Isoincidence plot obtained from 20 schlieren images. Features inside jet are visualized as dark-red islands of higher incidence, which represent stationary, or frequently occurring, features ($J = 3.8$, $S = 4.93$, and $M_c = 1.55$).

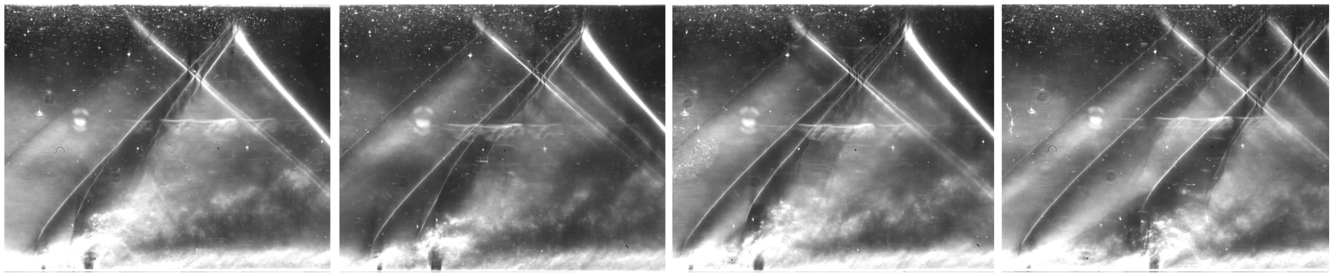

a) $J = 3.8$, $S = 3.59$ b) $J = 3.8$, $S = 4.48$ c) $J = 3.8$, $S = 5.38$ d) $J = 3.8$, $S = 9.87$

Fig. 11 Unprocessed schlieren images showing effect of variation in S at constant $J = 3.8$. Bow shocks merge closer to jet orifices for smaller S. Also, bow shocks merge closer to jet orifices for larger J. When bow shocks are sufficiently separated, then the two bow shocks behave independently. However, when they approach each other, then downstream bow shock changes shape. a) $J = 3.8$, $S = 3.59$, and $M_c = 1.55$. b) $J = 3.8$, $S = 4.48$, and $M_c = 1.55$. c) $J = 3.8$, $S = 5.38$, and $M_c = 1.55$. d) $J = 3.8$, $S = 9.87$, and $M_c = 1.55$.

[19] showed that the oscillatory character of the bow shock is imparted by the large-scale flow features inside the jet.

The location of the merger point is considered as a function of J and S. The experiments were performed for $M_c = 1.55 \pm 0.02$, $J \in [2.8, 3.8]$, and $S \in [3.59{:}9.87]$ and one extra condition for $J = 4.8$ and $S = 5.38$. Only for the cases $J = 2.8$ and $S \in [3.59, 4.48]$, for $J = 3.8$ and $S \in [3.59, 4.48, 4.93]$, and for $J = 4.8$ and $S = 5.38$, the bow shocks merged. The position of the merger point is obtained from snapshots of 20 images per (J, S) combination.

Remarkably, the location of the merger point is always found on the upstream bow shock, with the precise position depending on the specific (J, S) combination. The location of the merger point is found to vary within a certain range around its time-averaged location $(\xi, \eta) = (x/D_t + S, y/D_t)$ which is indicated by the red marker in Figs. 12 and 13 (range of $[-1.90D_t, 1.83D_t]$ along the upstream bow shock, with variance of $0.567D_t$). This excursion around the time-averaged location is due to the fluctuation of the downstream bow shock (see Fig. 12). The origin of the coordinates (ξ, η) is located at the center of the upstream orifice so that $\xi = S$ is at the center of the downstream orifice.

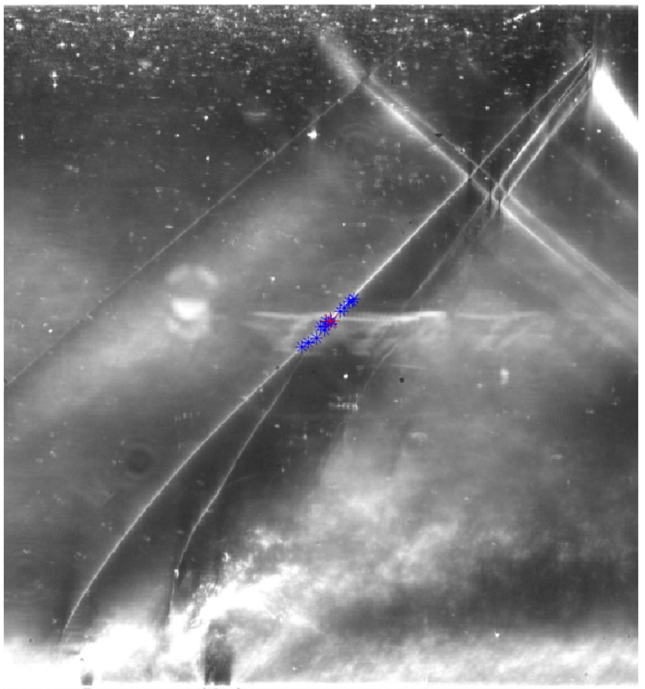

Fig. 12 Determination of location merger point from 20 images. The merger point is indicated by blue asterisks. The red asterisk indicates the time-averaged position of merger points ($J = 3.8$, $S = 4.93$, and $M_c = 1.55$).

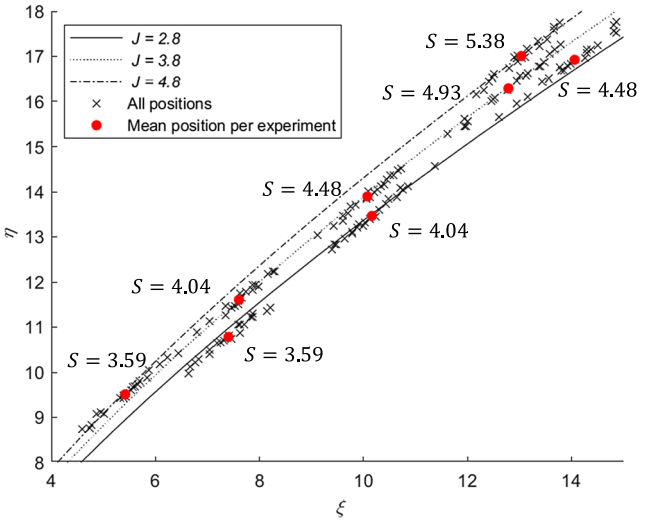

Fig. 13 Position of merger point for all (J, S) combinations (×), and their mean position per (J, S) combination (●). ($M_c = 1.55$). Included are predictions of Eq. (4) for $J \in$ [2.8,3.8,4.8].

Analysis shows that the time-averaged values of ξ and η behave as power-law functions of J and S. The coefficients in these functions were determined by least-squares fitting. The result is

$$\xi(J, S) = 0.633 J^{-1.066} S^{2.789}$$
$$\eta(J, S) = 1.924 J^{-0.572} S^{1.827} \quad (4)$$

In terms of $\eta = \eta(\xi; J)$ and $\eta = \eta(\xi; S)$, the following iso-J and iso-S functions are obtained, respectively:

$$\eta(\xi; J) = 2.596 J^{0.126} \xi^{0.655}$$
$$\eta(\xi; S) = 2.459 S^{0.331} \xi^{0.537} \quad (5)$$

In Eq. (4), the fit for $\xi(J, S)$ has a coefficient of determination $R^2 = 0.997$, and the fit for $\eta(J, S)$ has an R^2 value of 0.993. Therefore, it is concluded that both fits are acceptable. These relations are valid for $J \in [2.8{:}4.8]$, $S \in [3.59{:}5.38]$, $M_c = 1.55$ and are limited by the height of the test section, in other words, $\eta \leq 19.3$, and the boundary-layer thickness, $\eta \geq 2$. The variance of the merger point along the upstream bow shock is found to be $0.567D_t$, whereas the variance perpendicular to the upstream bow shock is $0.01D_t$. For more detailed results, see the work by Smink [17].

No significant effect of the merging of the bow shocks on the penetration of the jet (Sec. III.B) was observed.

B. Characteristics of Jet Upper Shear Layer

This section describes the results for the location of the jet upper shear layer. Figure 6 already showed the schlieren image for a reference case of dual-jet injection. The data derived from the schlieren images have been investigated for $J \in [2.8, 3.8, 4.8]$ and $S \in [0{:}9.87]$ at $M_c = 1.55 \pm 0.02$, all for a total orifice diameter $D_t = \sqrt{5}$ mm. In the horizontal direction, the area captured by the schlieren images is approximately $-9 \le x/D_t \le 20$, similar to the range of the images captured by de Maag et al. [2,5]. In the numerical studies of Lee [3] and Landsberg [4], a larger domain ($-10 \le x/D_t \le 35$ and $-10 \le x/D_t \le 50$, respectively) was considered, so the focus of their research was more on the character of the jet farther downstream. In the present study, the focus is on the near field of the jet injection.

For every (J, S) combination, 20 subsequent schlieren images were extracted from the database and postprocessed as described in Sec. II.B. Figure 10 shows the isoincidence plot in which the jet plume is determined for the domain $-1 \le x/D_t \le 15$. In the isoincidence plots, a higher value of the incidence is indicated by a color a value of 20. Therefore, more dominant, either stationary or frequently occurring, features, such as the barrel shock, can easily be identified by their color. Qualitative analysis of the various schlieren images in Figs. A1–A3 in the Appendix shows that dual-jet injection ($S \neq 0$) features stronger penetration of the jet into the crossflow than single-jet injection ($S = 0$). In addition, at constant J, penetration has a maximum for a specific value of S, as expected from literature [3]. The results of de Maag et al. [2] show that the value of S at which the maximum penetration occurs depends on J.

From the results, in line with findings in the literature, at constant S, the penetration increases with increasing J. The point of merger of the two bow shocks, as described in Sec. III.A, did not have a significant direct effect on the penetration depth, for the range of J and S considered in the present study; therefore, it does not need to be considered further as variable of interest for the penetration of the jet. Besides, it was observed that large-scale coherent roller-type features are present in the jet upper shear layer; see, e.g., Figs. A1–A3 in the Appendix. These features appear to be periodic, which might be an indication of a Kelvin–Helmholtz (KH) type of instability in the jet upper shear layer. However, the KH phenomenon is observed not equally clear in all schlieren images. A further in-depth experimental study into this specific phenomenon and its role in the mixing process is recommended. Verification of the presence of KH instability would provide the opportunity to use the knowledge of the physics of the KH instability in deriving a relation for the vertical spreading of the jet plume around its time-averaged position and therewith of the mixing.

1. *Location of Jet Upper Shear Layer*

The penetration of the jet into the crossflow is characterized by the (time-averaged) location of the upper shear layer. Adequate penetration of the jet upper shear layer is paramount for a good mixing of the gas in the jet with the gas in the crossflow. For every snapshot, at a number of x/D_t's, the maximum y coordinate of the shear layer is determined, and combining the data from 20 snapshots results in the data set for fitting a time-averaged location $y(x)$ of the shear layer. How to arrive at a general empirical similarity relation for the location of the upper shear layer of the jet has been investigated. For this purpose, in the literature, power-law functions were used for both single and dual-jet injection [2,8,11,20]. For the present research, the time-averaged location $y(x)$ of the jet upper shear layer in the near field downstream of the jet orifice is described by the function

$$\frac{y}{D_t}\left(\frac{x}{D_t}\right) = c_1\left(\left(\frac{x}{D_t} - c_3\right)^{c_2} + c_4\right) \tag{6}$$

with c_1, c_2, c_3, and c_4 coefficients depending on J and S. Preceding studies, e.g., those by de Maag et al. [2] and Gruber [11], used this function, but with $c_4 = 0$. In the present study, it appears that the coefficients $c_i(J, S)$ are more universal for the case $c_4 \neq 0$ included in the function. For determining the parameters $c_i(J, S)$, a least-squares fit is based on the data acquired for the location of the jet upper shear layer. The resulting fits for all values of S with $J = 2.8$ and 3.8 are of proper quality, in other words, $0.70 \le R^2 \le 0.85$. Details are presented in Ref. [16].

A global measure for the penetration depth is y_{avg}/D_t, just a single value, which is the value obtained by spatially averaging $y(x/D_t)$ over a certain range of x/D_t. The chosen range is from a position slightly downstream of the downstream jet orifice ($x/D_t = 0.5$) (because here the jet clearly turns toward streamwise direction) to a point farther downstream ($x/D_t = 15$). The average penetration depth is defined as

$$\begin{aligned}\frac{y_{\text{avg}}}{D_t}(J,S) &\equiv \frac{1}{14.5}\int_{0.5}^{15}\frac{y}{D_t}\left(\frac{x}{D_t}\right)d\left(\frac{x}{D_t}\right)\\ &= \frac{1}{14.5}\frac{c_1}{c_2+1}\left[(15-c_3)^{c_2+1} - (0.5-c_3)^{c_2+1}\right] + c_1c_4\end{aligned} \tag{7}$$

This measure gives a clear and consistent indication of the relative magnitude of the depth of penetration.

Based on these fits, similarities between the different fits for different values of S and J are sought. With the requirement that the coefficients of determination should be in the range $0.65 \le R^2 \le 0.85$ and the maximum deterioration in the value of R^2 is allowed to be 0.05, it was found that c_2, c_3, and c_4 are approximately constant for all combinations of J and S considered. Consequently, only c_1 needs to be considered as a function of J and S. For constant J, $c_1(J, S)$ appeared to be a Gaussian function; see [16] for a more elaborate description. Finally, the empirical similarity relation for the time-averaged location of the jet upper shear layer as function of x/D_t, S and J (based on data for $S \in [0{:}9.87]$ and $J \in [2.8, 3.8]$) was found to be

$$\begin{aligned}\frac{y}{D_t}\left(\frac{x}{D_t}; J, S\right) &= 0.432J^{0.461}\left\{2 + e^{-(1/2)[(S-4.732J^{0.288})/6.103J^{-0.521}]^2}\right\}\\ &\times\left[\left\{\left(\frac{x}{D_t}\right) + 0.68\right\}^{0.333} + 0.80\right]\end{aligned} \tag{8}$$

The coefficient of determination of $R^2 = 0.739$ calculated for this fitting function, calculated for all data acquired, is considered

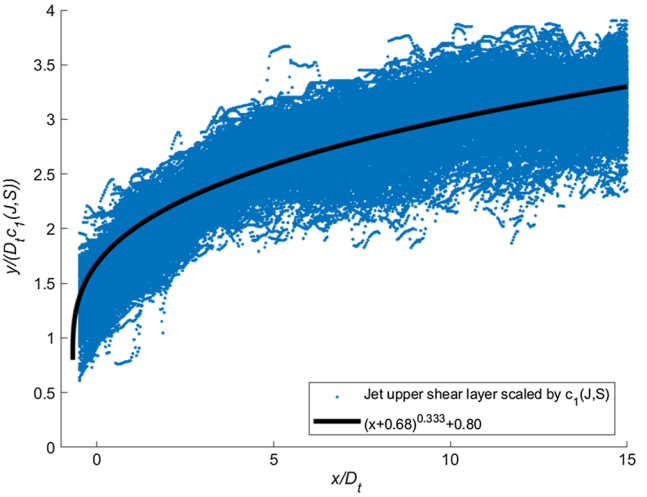

Fig. 14 Instantaneous location of upper shear layer jet from schlieren images (blue) and empirical similarity relation for time-averaged location (Eq. (8), black), both scaled with $c_1(J,S)$ [see Eqs. (6) and (8)] for $J = [2.8,3.8]$, $S \in [0{:}9.87]$, $M_c = 1.55$. Data obtained from 20 schlieren images per (J, S) combination, total of 22×20 images. Each schlieren image provides ±350 data points.

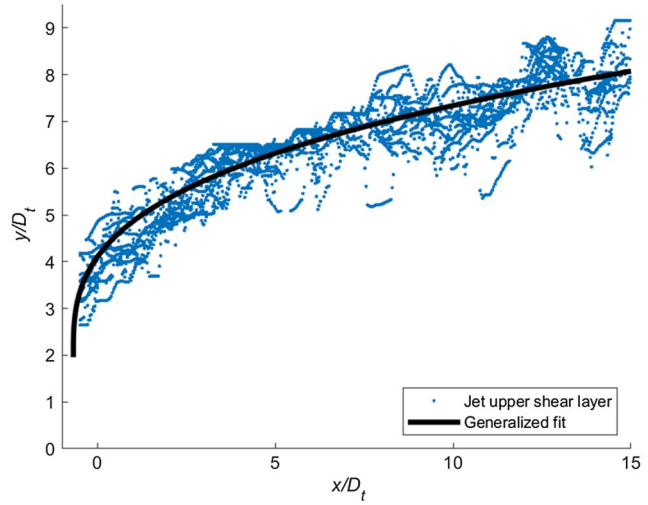

Fig. 15 Instantaneous location of upper shear layer jet from schlieren images (blue) and empirical similarity relation for time-averaged location [Eq. (8), black] for $J = 4.8$, $S = 5.38$, and $M_c = 1.55$. Data obtained from 20 schlieren images per (J, S) combination.

Table 2 Results for c_1 determined from least-squares fit, compared with results from Eq. (8), together with coefficient of determination R^2, for $J = 4.8$, $S \in [0,5.38]$, and $M_c = 1.55$

		Based on least-squares fit		Based on Eq. (8)	
Conditions		c_1	R^2	$c_1(J,S)$	R^2
$J = 4.8$	$S = 0$	1.804	0.680	1.800	0.680
	$S = 5.38$	2.424	0.842	2.447	0.840

to be acceptable; see also Fig. 14. The variance calculated from the data $(x/D_t, y/D_t)$ and Eq. (8) is equal to 0.352. Using Eq. (7), the average penetration depth calculated from the empirical similarity relation is

$$\frac{y_{\text{avg}}}{D_t}(J,S) = 1.194J^{0.461}\left\{2 + e^{-(1/2)[(S-4.732J^{0.288})/6.103J^{-0.521}]^2}\right\} \quad (9)$$

From Eqs. (8) and (9), it follows that, at constant J, the maximal penetration occurs at $S_{\text{opt}} = 4.732J^{0.288}$ and is equal to $(y_{\text{avg}}/D_t)(J, S_{\text{opt}}) = 3.582J^{0.461}$.

2. *Discussion on Location of Jet Upper Shear Layer*

For validation of the empirical similarity relation, Eq. (8), for values of J higher than $J = 2.8$ and 3.8, the results for $J = 4.8$ and $S \in [0, 5.38]$ have been used. Figure 15 presents results from Eq. (8) for the time-averaged location of the upper shear layer of the jet, with the instantaneous location of the upper shear layer of the jet (marked as blue dots) obtained from the schlieren images for $J = 4.8$ and $S = 5.38$; see also Table 2.

From Table 2, the values for $c_1(J, S)$ as determined from Eqs. (6) and (8) closely approach the value determined by the least-squares fit. Both fits achieve coefficients of determination R^2 which are very similar and also similar to R^2 determined for other (J, S) combinations for single-jet and dual-jet injection. For a more elaborate analysis of the quality of the fits, see the work by Smink [17].

These results prove that the empirical similarity relation [Eq. (8)] appropriately describes the time-averaged location of the upper shear layer of the jet as a function of (x/D_t), J, and also S. However, still some questions remain to be addressed.

For $S = 0$, there is only one orifice with diameter D_t. For small and moderate values of S, the downstream jet will be located in the so-called quasi-stagnant zone of the flowfield of the upstream jet. For higher values of S, the downstream jet enters the zone of reattaching supersonic flow of the upstream jet. Therefore, the larger the value of S is, the more possibilities the flow has to recover from subsonic to supersonic flow. Then, for $S \to \infty$, the crossflow approaching the downstream jet will be recovered and will be not far from freestream conditions; therefore, the two jets will behave independently [3]. In that case, the minimum of $c_1(J, S)$ would correspond to the case of penetration of a single-jet with diameter D_2. In the present study, data for $S > 10$ were not acquired; therefore, it cannot be verified whether or not the empirical similarity relation is also an appropriate fit in this regime.

Other questions that remain are as follows. What is the difference between penetration for $S = 0$ and that for $S \to \infty$? What is the behavior of the upper shear layer of the jet for $S > 10$, and which

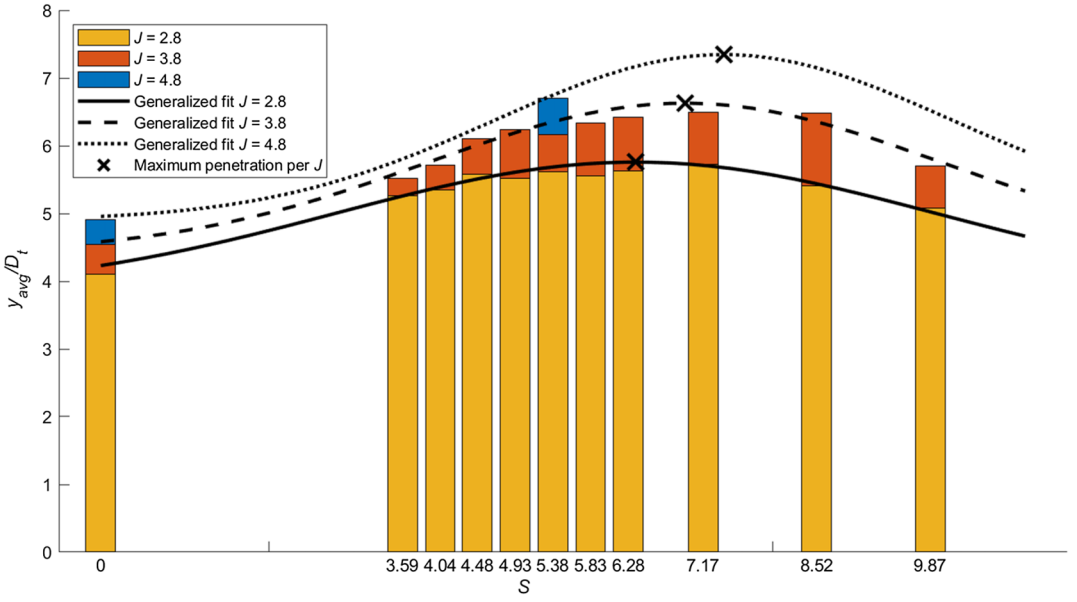

Fig. 16 Bar diagram: spatially and time-averaged penetration depth of upper shear layer of jet as calculated from individual least-squares fits using Eq. (6). Solid lines: spatially and time-averaged penetration depth calculated from Eq. (9). Optimal value (×) of S at constant J for maximal penetration depth equals $S_{\text{opt}} = 4.732J^{0.288}$ where y_{avg}/D_t equals $3.582J^{0.461}$. $M_c = 1.55$.

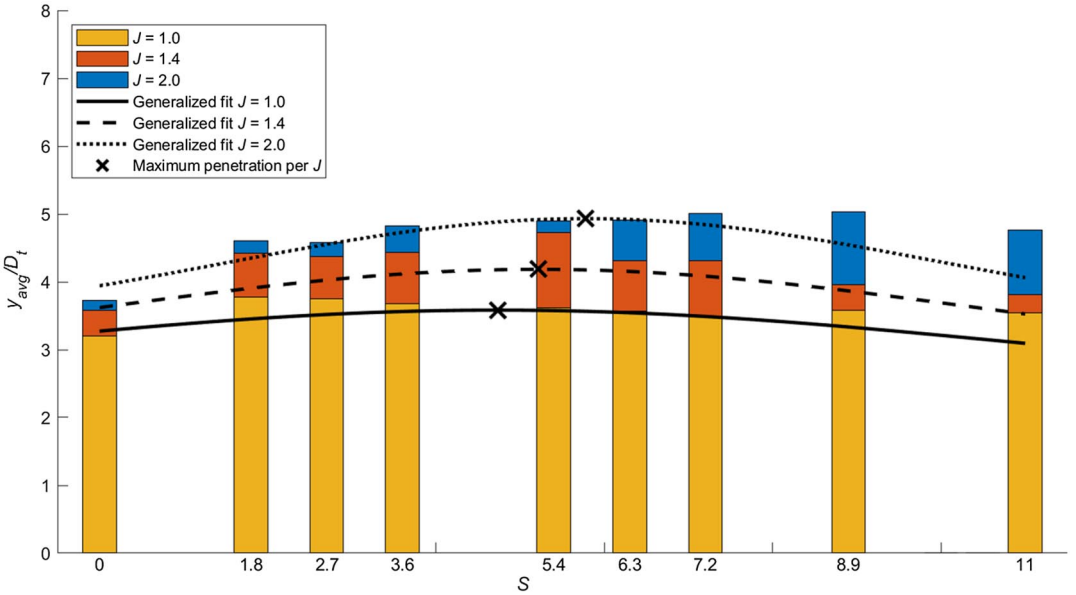

Fig. 17 Bar diagram: spatially and temporally averaged penetration depth in domain ($0.5 \leq x/D_t \leq 15$) from experiments by de Maag [2]. Solid lines: average penetration depth calculated from Eq. (9). The maximal penetration depth (×) is calculated from $S_{\text{opt}} = 4.732J^{0.288}$, where y_{avg}/D_t equals $3.582J^{0.461}$. $M_c = 1.6$.

distance S between the jet orifices is large enough so that the jets do not affect each other? More importantly, is it actually possible to combine results for the location of the jet upper shear layer for single-jet injection and those for dual-jet injection, or is the behavior of dual-jet injection fundamentally different? Still, for the range ($0 \leq S \leq 10$) considered in the present study, the scaling using the empirical similarity relation given in Eq. (8) yields quite acceptable results [the maximum relative difference between Eq. (8) and individual results is 3%; see Fig. 16].

As an overview of all results obtained, Fig. 16 presents the spatially and time-averaged penetration depth y_{avg}/D_t, see Eq. (9), for each (J, S) combination considered in the present study. The average penetration depth is determined from the individual least-squares fits as well as by directly integrating the empirical similarity relation, Eq. (8), for $J \in [2.8, 3.8, 4.8]$ using the analytical evaluation of Eq. (7), resulting in Eq. (9). Figure 16 shows that the spatially and temporally averaged penetration depth y_{avg}/D_t of the upper shear layer of the jet is described appropriately: trends are predicted correctly within 3% relative difference. So, in conclusion, these results indicate that Eq. (8) is an appropriate empirical similarity relation for predicting the time-averaged location of the jet upper shear layer for a wide range of parameters.

This is confirmed by the data acquired by de Maag et al. [2], for lower values of J, namely, in the range $J = [1.0, 1.4, 2.0]$. These data validate Eq. (8), the empirical similarity relation for the spatially and time-averaged location of the upper jet shear layer. Figure 17 shows the averaged penetration depth y_{avg}/D_t obtained from Ref. [2] with the average penetration depth calculated from Eq. (9).

The empirical similarity relation, Eq. (8), follows the correct trend, with a maximal relative deviation of 17% from the bars in Fig. 17, which is based on experiments from Ref. [2]. De Maag investigated penetration of single and dual-jet injection into a supersonic crossflow at a slightly higher Mach number of $M_c = 1.6$. Therefore, some small differences are to be expected. Also, some deviations are accounted for by the different method of data acquisition, visual versus semi-automatic, and the smaller number of images used by de Maag et al. [2], namely, 3 or 4 rather than 20, per combination of J and S. It should also be noted that the injection orifices in the injection blocks used by de Maag had rounded-off edges, whereas in the present experimental setup, care has been taken to ensure that the edges of the orifices are sharp, resulting in a sonic jet with a compacter expansion fan. Nevertheless, the trends found using the empirical similarity relation Eq. (8) as developed in the present study are considered to be validated by the results of de Maag.

IV. Conclusions

The merger point of the two bow shocks arising in front of the two sonic jets injected into the supersonic crossflow oscillates with amplitude of approximately $1.9D_t$. This is caused mostly by the oscillation of the downstream bow shock due to the disturbed flowfield induced by the upstream bow shock. Therefore, when the two shocks are close enough to merge, the location of the merger point oscillates accordingly. The time-averaged position of this merger point has been described using a power-law function of the jet-to-crossflow momentum flux ratio J and the dimensionless distance S between the two orifices. It has been found that the oscillating position of the merger point does not appear to affect the penetration depth of the jet very much.

The time-averaged depth of penetration y/D_t of the upper shear layer of the jet is a function of coordinate x/D_t, and parameters J and S. Compared to single-jet injection, the depth of penetration is enhanced by dual-jet injection. At constant S, the penetration depth increases with increasing J, while at constant J, S has an optimal value S_{opt} at which the penetration depth is maximal. S_{opt} increases with increasing J, while the value of the averaged depth of penetration at S_{opt} also increases with J.

The time-averaged location of the upper shear layer of the jet has been described by a four-coefficient least-squares fit of data obtained, through a semi-automatic processing algorithm, from 20 schlieren images per (J, S) combination. The specific expression for the fit is based on searching for an expression for which most of the coefficients are invariant for most (J, S) combinations ($J = [2.8, 3.8, 4.8]$, $S \in [0{:}9.87]$). The fits are converted into an empirical similarity relation in terms of J and S. The spatially averaged, temporally averaged penetration depth at constant J, based on least-squares fits of the data, as well as on similar fits from preceding studies, corresponds closely with the spatially averaged penetration depth calculated from the empirical similarity relation, a compound function of J and S.

For investigating the validity of the empirical similarity relation for the time-averaged location of the upper shear layer of the jet for a larger range of J and of S, experiments for additional (J, S) combinations should be carried out. In addition, the effect of the crossflow Mach number M_c on the penetration of the jet(s) should be subject of study in order to also include M_c in a generalized empirical similarity relation for the time-averaged location of the upper shear layer of the jet achieved in tandem dual sonic-jet injection.

Appendix: Unprocessed Schlieren Images

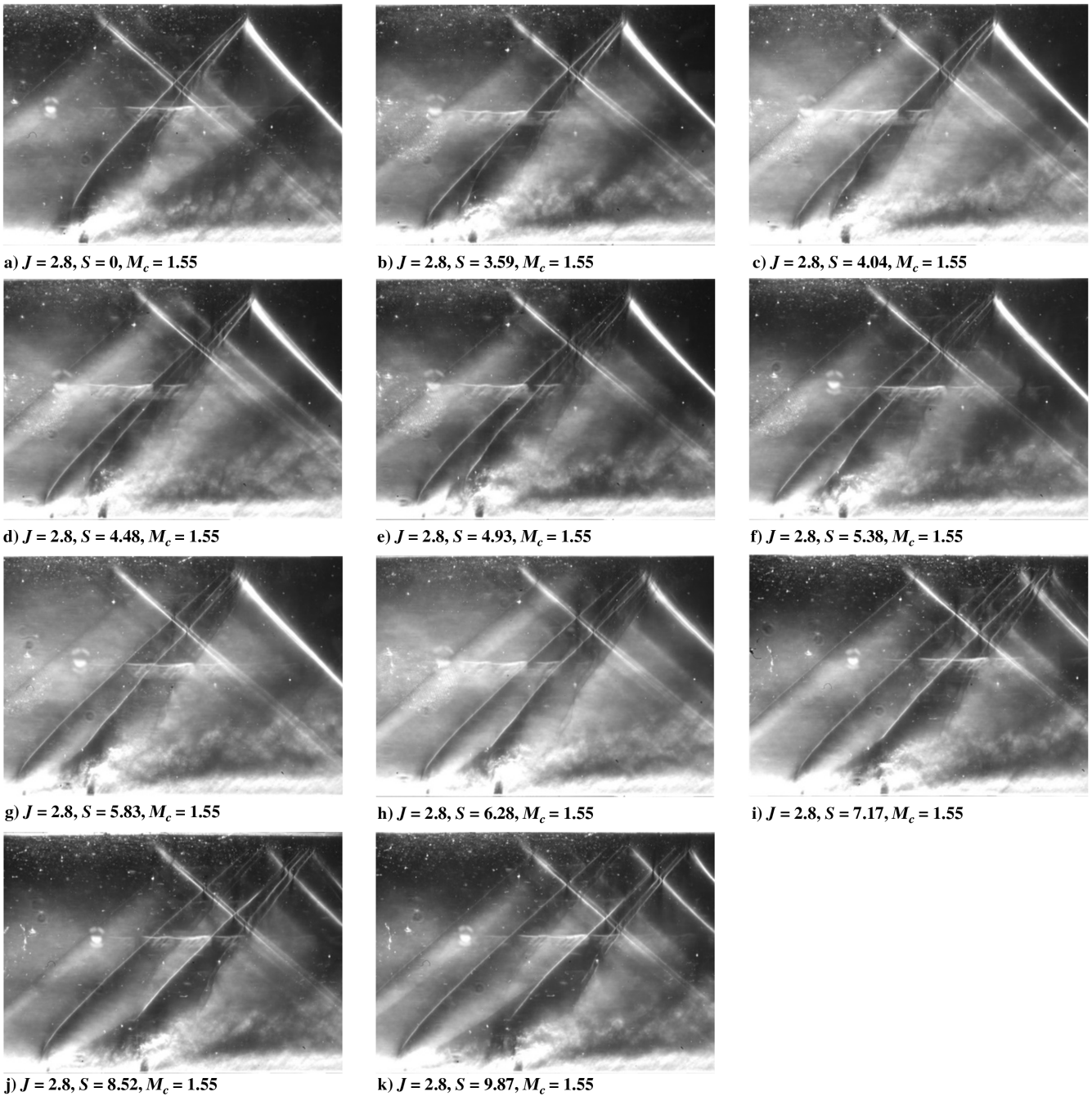

a) $J = 2.8$, $S = 0$, $M_c = 1.55$ b) $J = 2.8$, $S = 3.59$, $M_c = 1.55$ c) $J = 2.8$, $S = 4.04$, $M_c = 1.55$

d) $J = 2.8$, $S = 4.48$, $M_c = 1.55$ e) $J = 2.8$, $S = 4.93$, $M_c = 1.55$ f) $J = 2.8$, $S = 5.38$, $M_c = 1.55$

g) $J = 2.8$, $S = 5.83$, $M_c = 1.55$ h) $J = 2.8$, $S = 6.28$, $M_c = 1.55$ i) $J = 2.8$, $S = 7.17$, $M_c = 1.55$

j) $J = 2.8$, $S = 8.52$, $M_c = 1.55$ k) $J = 2.8$, $S = 9.87$, $M_c = 1.55$

Fig. A1 Unprocessed schlieren images for $J = 2.8$ and all values of S considered. $M_c = 1.55$. For every (J, S) combination, one of the 20 images available is shown.

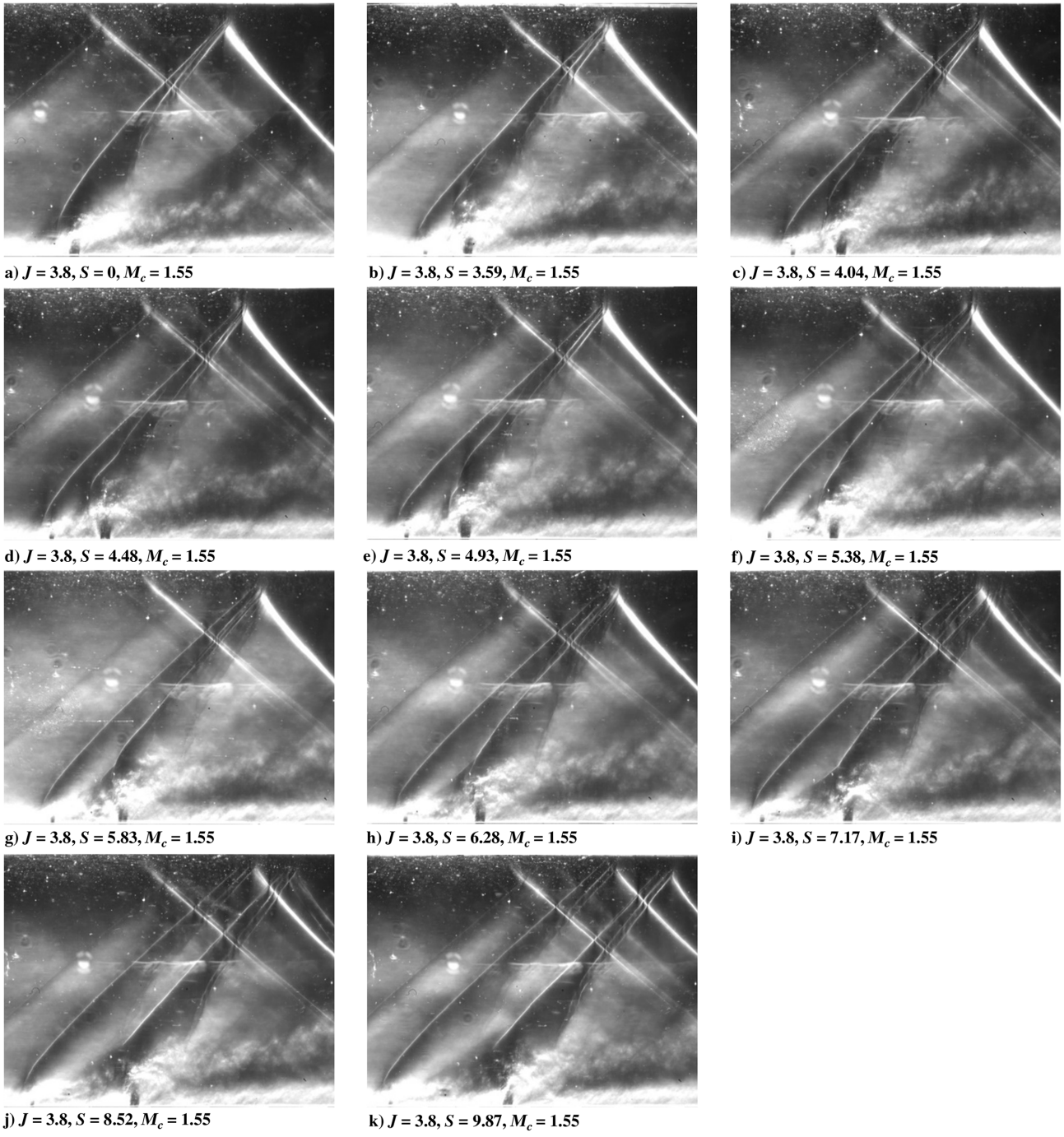

a) $J = 3.8$, $S = 0$, $M_c = 1.55$ b) $J = 3.8$, $S = 3.59$, $M_c = 1.55$ c) $J = 3.8$, $S = 4.04$, $M_c = 1.55$

d) $J = 3.8$, $S = 4.48$, $M_c = 1.55$ e) $J = 3.8$, $S = 4.93$, $M_c = 1.55$ f) $J = 3.8$, $S = 5.38$, $M_c = 1.55$

g) $J = 3.8$, $S = 5.83$, $M_c = 1.55$ h) $J = 3.8$, $S = 6.28$, $M_c = 1.55$ i) $J = 3.8$, $S = 7.17$, $M_c = 1.55$

j) $J = 3.8$, $S = 8.52$, $M_c = 1.55$ k) $J = 3.8$, $S = 9.87$, $M_c = 1.55$

Fig. A2 Unprocessed schlieren images for $J = 3.8$ and all values of S considered. $M_c = 1.55$. For every (J, S) combination, one of the 20 images available is shown.

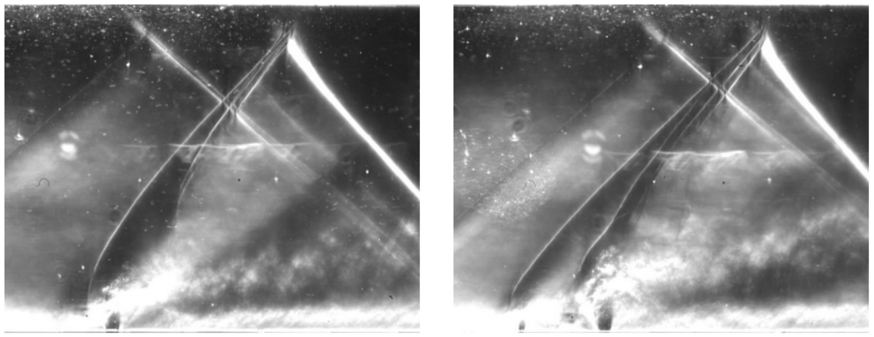

a) $J = 4.8$, $S = 0$, $M_c = 1.55$ b) $J = 4.8$, $S = 5.38$, $M_c = 1.55$

Fig. A3 Unprocessed schlieren images for $J = 4.8$ and the two values of S considered. $M_c = 1.55$. For every (J, S) combination, one of the 20 images available is shown.

Acknowledgments

The authors would like to thank W. Lette for his technical support with the experimental setup and during the measurements. Also, the authors are grateful for the Vertical-Cavity-Surface-Emitting Laser light source manufactured by F.B. Segerink from the Optical Sciences group at the University of Twente.

References

[1] Fry, R. S., "A Century of Ramjet Propulsion Technology Evolution," *Journal of Propulsion and Power*, Vol. 20, No. 1, 2004, pp. 27–58. https://doi.org/10.2514/1.9178

[2] de Maag, S., Hoeijmakers, H. W. M., Venner, C. H., Segerink, F. B., and Offerhaus, H. L., "Investigation of Tandem Injection in Supersonic Flow Using Schlieren Visualization," *AIAA SciTech 2020 Forum*, AIAA Paper 2020-0040, Jan. 2020. https://doi.org/10.2514/6.2020-0040

[3] Lee, S. H., "Characteristics of Dual Transverse Injection in Scramjet Combustor, Part 1: Mixing," *Journal of Propulsion and Power*, Vol. 22, No. 5, 2006, pp. 1012–1019. https://doi.org/10.2514/1.14180

[4] Landsberg, W. O., Wheatley, V., and Veeraragavan, A., "Characteristics of Cascaded Fuel Injectors Within an Accelerating Scramjet Combustor," *AIAA Journal*, Vol. 54, No. 12, 2016, pp. 3692–3700. https://doi.org/10.2514/1.J054815

[5] de Maag, S., "Schlieren Flow Visualization for Cascaded Injection in Supersonic Flow Employing Power VCSEL Light Sources," M.Sc. Thesis EFD-314, Univ. of Twente, Enschede, The Netherlands, 2019.

[6] Schetz, J. A., and Billig, F. S., "Penetration of Gaseous Jets Injected into a Supersonic Stream," *Journal of Spacecraft and Rockets*, Vol. 3, No. 11, 1966, pp. 1658–1665. https://doi.org/10.2514/3.28721

[7] Papamoschou, D., and Hubbard, D., "Visual Observations of Supersonic Transverse Jets," *Experiments in Fluids*, Vol. 14, May 1993, pp. 468–476. https://doi.org/10.1007/BF00190201

[8] Portz, R., and Segal, C., "Penetration of Gaseous Jets in Supersonic Flows," *AIAA Journal*, Vol. 44, No. 10, 2006, pp. 2426–2429. https://doi.org/10.2514/1.23541

[9] Ben-Yakar, A., and Hanson, R. K., "Ultra-Fast-Framing Schlieren System for Studies of the Time Evolution of Jets in Supersonic Crossflows," *Experiments in Fluids*, Vol. 32, April 2002, pp. 652–666. https://doi.org/10.1007/s00348-002-0405-z

[10] Gruber, M. R., Nejad, A. S., Chen, T. H., and Dutton, J. C., "Mixing and Penetration Studies of Sonic Jets in a Mach 2 Freestream," *Journal of Propulsion and Power*, Vol. 11, No. 2, 1995, pp. 315–323. https://doi.org/10.2514/3.51427

[11] Gruber, M. R., Nejad, A. S., Chen, T. H., and Dutton, J. C., "Transverse Injection from Circular and Elliptic Nozzles into a Supersonic Crossflow," *Journal of Propulsion and Power*, Vol. 16, No. 3, 2000, pp. 449–457. https://doi.org/10.2514/2.5609

[12] Rothstein, A. D., and Wantuck, P. J., "A Study of the Normal Injection of Hydrogen Into a Heated Supersonic Flow Using Planar Laser-Induced Fluorescence," *28th Joint Propulsion Conference and Exhibit*. AIAA Paper 1992-3423, July 1992.

[13] Settles, G. S., *Schlieren and Shadowgraph Techniques*. Springer-Verlag, Heidelberg, 2001, pp. 25–28, 32–33.

[14] Lerink, C. W., de Maag, S., and Hoeijmakers, H. W. M., "Shear Layer Analysis for Transverse Sonic Injection in Supersonic Cross-Flow Using VCSEL Schlieren Imaging," Univ. of Twente, EFD-411, Enschede, The Netherlands, 2020 (unpublished).

[15] Kouchi, T., Hoshino, T., Sasaya, K., and Masuya, G., "Time-Space Trajectory of Unsteady Jet into Supersonic Crossflow Using High-Speed Framing Schlieren Images," *16th AIAA/DLR/DGLR International Space Planes and Hypersonic Systems and Technologies Conference*, AIAA Paper 2009-7316. Oct. 2009.

[16] Smink, J. S., Hoeijmakers, H. W. M., and Venner, C. H., "Investigation Behavior Jet Shear Layer in Tandem Dual Jet Injection in Supersonic Crossflow from Schlieren Images," *AIAA SciTech 2022 Forum*, AIAA Paper 2022-2565, Jan. 2022. https://doi.org/10.2514/6.2022-2565

[17] Smink, J. S., "Investigation of Behaviour of Jet Shear Layer in Tandem Dual Jet Injection in Supersonic Crossflow Using Schlieren Images," M.Sc. Thesis EFD-357, Univ. of Twente, Enschede, The Netherlands, 2020.

[18] Giskes, E., "Design and Optimization of a LED Driven Ultra-Fast Schlieren Imaging Set Up to Investigate a Sonic Jet in Supersonic Crossflow," M.Sc. Thesis EFD-228, Univ. of Twente, Enschede, The Netherlands, 2015.

[19] Gruber, M. R., Nejad, A. S., Chen, T. H., and Dutton, J. C., "Bow Shock/Jet Interaction in Compressible Transverse Injection Flowfields," *AIAA Journal*, Vol. 34, No. 10, 1996, pp. 2191–2193. https://doi.org/10.2514/3.13372

[20] Gruber, M. R., Nejad, A. S., Chen, T. H., and Dutton, J. C., "Compressibility Effects in Supersonic Transverse Injection Flowfields," *Physics of Fluids*, Vol. 9, No. 5, 1997, pp. 1448–1461. https://doi.org/10.1063/1.869257

C. Lee
Associate Editor